

Journal of Geophysical Research: Solid Earth

RESEARCH ARTICLE

10.1029/2017JB014899

Key Points:

- The event nucleated at ~20-km depth and broke a >150-km-long segment of the Mesoamerican Subduction Zone, rupturing toward the NW
- There may have been a slip between the trench and coast as suggested by joint inversion of teleseismic records and near-field static offsets
- Another possibility is that there was coseismic slip near the trench and postseismic slip near the coast

Supporting Information:

- Supporting Information S1

Correspondence to:

V. Hjörleifsdóttir,
vala@igeofisica.unam.mx

Citation:

Hjörleifsdóttir, V., Sánchez-Reyes, H. S., Ruiz-Angulo, A., Ramírez-Herrera, M. T., Castillo-Aja, R., Singh, S. K., & Ji, C. (2018). Was the 9 October 1995 M_w 8 Jalisco, Mexico, earthquake a near-trench event? *Journal of Geophysical Research: Solid Earth*, 123. <https://doi.org/10.1029/2017JB014899>

Received 25 AUG 2017

Accepted 12 SEP 2018

Accepted article online 15 SEP 2018

Was the 9 October 1995 M_w 8 Jalisco, Mexico, Earthquake a Near-Trench Event?

Vala Hjörleifsdóttir¹ , H. S. Sánchez-Reyes² , Angel Ruiz-Angulo³ ,
Maria Teresa Ramírez-Herrera⁴ , Rocio Castillo-Aja⁵ , Shri Krishna Singh¹, and Chen Ji⁶ 

¹Departamento de Sismología, Instituto de Geofísica, Universidad Nacional Autónoma de México, Ciudad de México, México, ²University Grenoble Alpes, CNRS, ISTerre, Grenoble, France, ³Centro de Ciencias de la Atmósfera, Universidad Nacional Autónoma de México, Ciudad de México, Mexico, ⁴Laboratorio Universitario de Geofísica Ambiental, IGG, Universidad Nacional Autónoma de México, Ciudad Universitaria, Ciudad de México, Mexico, ⁵Posgrado en Geografía, Universidad Nacional Autónoma de México, Ciudad Universitaria, Ciudad de México, Mexico, ⁶Department of Earth Science, University of California, Santa Barbara, CA, USA

Abstract The behavior of slip close to the trench during earthquakes is not well understood, and observations of large earthquakes breaking the near trench fault surface are rare. The 1995 M_w 8.0 Jalisco earthquake seems to have broken the near-trench area, as evidenced by large M_s - M_w disparity, small high-frequency radiated energy compared to total energy, and low E_r/M_0 ratios, in addition to several finite slip models showing large slip near the trench. However, slip models obtained using campaign Global Positioning System data suggest slip near shore. In this study we try to answer whether this event was a near-trench event or not, by inverting teleseismic P , S , Rayleigh, and Love waves, as well as campaign Global Positioning System static offsets, either separately or jointly, to obtain the slip distribution on the fault as a function of time. We find two possible end-member scenarios consistent with observed data: (1) coseismic slip distributed between coast and trench and no (or very little) postseismic slip and (2) coseismic slip principally near the trench with large (up to 1.8 m) aseismic slip occurring in the first 5–10 days after the earthquake, with a total moment corresponding to 16% of that of the event. We are unable to distinguish between these two end-member scenarios by tsunami modeling and finally are neither able to conclude or exclude that the event was a typical near trench event.

1. Introduction

The shallowest portion of the mega thrust interface in subduction zones has lower seismicity than the interface further downdip and has been thought to accommodate the relative plate motion by creep (Byrne et al., 1988). However, in some regions, this portion of the interface breaks in so-called tsunami earthquakes (Kanamori, 1972; Lay et al., 2012), such as the Sanriku 1896 (Tanioka & Satake, 1996), Nicaragua 1992 (Kanamori & Kikuchi, 1993), Java 1994 (Polet & Thio, 2003), and Mentawai 2010 (Hill et al., 2012; Newman et al., 2011) earthquakes or participates in large megathrust events, with exceptionally large slip, as in the 2011 Tohoku earthquake (Ito et al., 2011; Sato et al., 2011; Shao et al., 2011; Simons et al., 2011).

There are many unanswered questions about the relative behavior of the friction on the fault between this shallowest portion of the subduction zone interface and the further downdip segment typically considered seismogenic, for example, what controls the apparent downdip segmentation? How does it vary between different subduction zones? Is the updip segment aseismically creeping in some zones? Can the updip portion break by itself, or do earthquakes have to nucleate and/or involve important slip in the downdip zone as well? The answers to these questions are important for the estimates of tsunami hazard as large slip in the updip zone produces a much larger tsunami than similar slip in the downdip zone. However, due to the long recurrence interval of large earthquakes and short time span of historical records, there are only a few regions where large earthquakes breaking the shallow parts of the interface have been observed.

Arguably, the clearest example of downdip segmentation is in the Japan Trench. Several earthquakes have broken the subduction interface during the last 150 years, notably by the 1896 Sanriku earthquake that is considered to have broken only the shallow part of the interface (Tanioka & Satake, 1996); the 1978 and 2005 Miyagi-Oki earthquakes, which broke the further downdip segment (Okada et al., 2005; Seno et al., 1980; Yamanaka & Kikuchi, 2004); and the 2011 Tohoku earthquake, which broke both the shallow and the

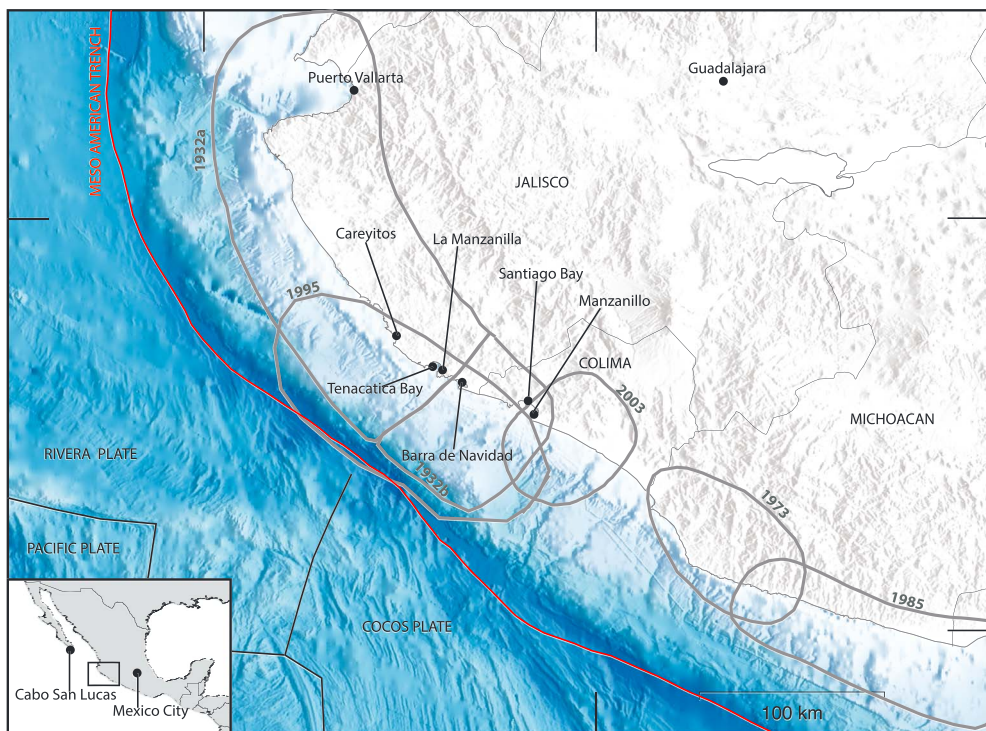


Figure 1. Tectonic context of the 1995 earthquake, as well as rupture areas of large earthquakes in the region (gray circles; 1973, Reyes et al., 1979; 1932, 2003, Singh et al., 1985, 2003; 1985, UNAM Seismology Group, 1986; 1995, Pacheco et al., 1997), localities referred to in text and plate boundaries (Bird, 2003).

deep parts of the subduction interface (Ammon et al., 2011; Simons et al., 2011) with an extraordinarily large slip of up to 60 m (Ito et al., 2011; Sato et al., 2011; Shao et al., 2011) on the shallow part. In this region, the near-trench area has also been observed to slip in episodic slow-slip events (Ito et al., 2015).

Not only can the updip portion of the fault accommodate relative motion across it by creep or episodic slow slip but so can the downdip portion, as well as some areas in the traditionally seismogenic zone (see, for example, Lay et al., 2012). The interpretation is that the friction on the fault interface varies from place to place (Pacheco et al., 1993).

In Mexico, the two largest subduction interface events recorded in the last 100 years, those of 3 June 1932, M_S 8.2 (Abe, 1981), and 9 October 1995, M_w 8.0 (GlobalCMT), broke the same lateral segment of the Mesoamerican Trench (Figure 1). Additionally, another large earthquake, the 18 June 1932, M_S 7.8 (Abe, 1981) event, broke the same segment. Several observations suggest that the 1932 and 1995 events were very different (Pacheco et al., 1997). High intensities and similar M_S (8.2) versus M_w (8.0) values were reported for the 1932 event (Anderson et al., 1989; Singh et al., 1985), whereas low intensities and a large discrepancy between m_b/M_S (6.6/7.4, U.S. Geological Survey [USGS]) versus M_w (8.0, GlobalCMT) for the 1995 event (Ortiz et al., 1998, 2000). These differences suggest that perhaps the 1995 event broke the shallower segment of the fault interface, whereas the 1932 event the deeper.

There is conflicting evidence from seismic (Mendoza & Hartzell, 1999; Mendoza et al., 2011; Ye et al., 2016, USGS Finite fault source model) and geodetic data (Hutton et al., 2001; Melbourne et al., 1997) on the location of the large slip during the 1995 event; the slip distributions obtained from seismic data show much shallower slip than those obtained from Global Positioning System (GPS) data. Both types of models have their uncertainties and resolution issues, but the question remains, can both data sets be predicted by the same model?

In this study we aim to reconcile the different locations of large slip areas obtained by inverting seismic and geodetic data for the Jalisco 1995 earthquake. To do so, we invert seismic and geodetic recordings separately, as well as jointly. We find two possible scenarios: (1) a joint model with fairly uniform and purely coseismic slip

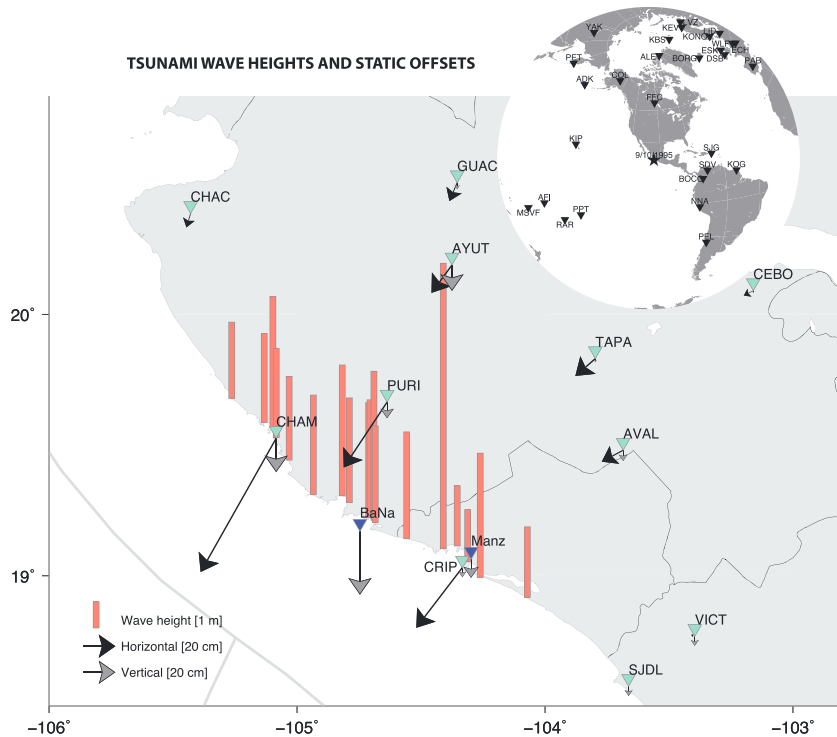


Figure 2. Data used in this study observed static displacements measured at Global Positioning System stations (aquamarine triangles), subsidence measured at pressure gauges (blue triangles), post tsunami field survey runup height estimates (peach bars), and seismic stations (black triangles on inset).

between coast and trench and (2) coseismic slip principally near the trench and aseismic slip (slow slip or afterslip) in the 6 months before or 5–10 days after the event, downdip of the coseismic slip. The tsunami wave height expected for each of the models is calculated and compared with tsunami observations in an attempt to set further constraints on the source model.

2. Seismic Source Modeling: Data and Methods

2.1. Teleseismic Data

Several digital, teleseismic, broadband recordings of the 1995 Jalisco earthquake are available. In this study we used *P* and *S* waves registered at 27 and 17 stations, respectively, with a relatively good azimuthal distribution, given the lack of high-quality stations in the Pacific basin (Figure 2). Furthermore, we use Rayleigh and Love waves registered at 17 and 13 stations, respectively. The stations are located at angular distances of 32 to 89° from the hypocenter.

The *P* and *S* wave arrival times are picked manually, to remove the effect of 3-D structure along their trajectories on the traveltimes of the waves. Considerable care was taken in this step to assure that all stations were aligned on the same phase. We deconvolved the instrument responses from the original records, resulting in displacement seismograms, which we subsequently band-passed between 1–100 s for the body wave records and 170–250 s for the surface-wave seismograms.

2.2. Static Displacements

The 1995 Jalisco earthquake is one of the first large earthquakes for which coseismic displacements were measured by GPS instruments. A campaign survey that measured locations of 11 sites in the Jalisco-Colima area was carried out in March/April of 1995. The sites were reoccupied 5–10 days after the 9 October earthquake (Melbourne et al., 1997), roughly 6 months after the initial measurement. Coseismic displacement vectors were calculated by Melbourne et al. (1997) and Hutton et al. (2001). Both studies included 5–10 days of postseismic displacement in their estimates of coseismic displacement, due to the time

spent to reoccupy the stations, as well as the aforementioned 6 months of preseismic displacements. In this study we mostly use the displacement vectors estimated by the second group Hutton et al. (2001) as they considered more precise orbits for the calculations; however, the differences are not large between the two sets of estimated displacement vectors, and we will show that our results are minimally affected by this choice.

2.3. Subsidence and Strong Motion Records

The observed subsidence at a tide gauge in Manzanillo harbor and on pressure sensors slightly offshore Barra de Navidad show subsidence of 11.8 ± 1.3 cm and 40 ± 2 cm, respectively (Ortiz et al., 2000). We note that these observations were not used in previous geodetic studies and the subsidence estimate from the tide gauge corresponds to deformation during a different time window than the GPS data, making a direct comparison difficult. For these reasons we have not included the data points in the inverse modeling, but rather forward predicted the subsidence values at the Barra de Navidad site, to compare with our models for reference. The Manzanillo harbor site is very close to the CRIP GPS site.

Records from five accelerographic stations are available for this earthquake. Unfortunately, none of the stations are located within a fault length of the earthquake, and they were located on or near dams, with near-station effects heavily influencing the movements. Therefore, we do not use these stations for the modeling.

2.4. Inversion Method

We invert the observed motions for the distribution of slip on the fault plane during the earthquake. The inversion is performed using the Fast Finite Fault (FFF) inversion algorithm (Ji et al., 2002a, 2002b). The algorithm uses a simulated annealing method, which minimizes the weighted difference between wavelet coefficients of observed and simulated seismograms. The slip on each subfault has an asymmetric time function (Ji et al., 2003), and smoothing is applied both to the slip distribution and to the rupture contours (Shao et al., 2011). Static offsets cannot be modeled by wavelets and are included in the misfit function by a simple difference between observed and modeled displacements.

Several subjective choices of input parameters are necessary for the modeling. First, the size and orientation of the fault plane have to be fixed. The strike is relatively well determined by the orientation of the subduction zone, but an error in the dip angle can have an important effect on the solution. We use the dip of 13° in this study, as an intermediate between the dip of the GlobalCMT solution (9°) and the dip of the slab model Slab1.0, which is $10\text{--}20^\circ$ in this region (Hayes et al., 2012). The rake is allowed to vary within $\pm 45^\circ$ from an average rake of 90° . The weights put on the misfit of scalar moment, and the solution roughness is also important. However, amplitudes of surface waves are very sensitive to the scalar moment and when included in the inversion the weight on the scalar moment becomes unimportant. For reference we compare to the moment of the GlobalCMT solution, $M_{0_ref} = 1.15 * 10^{21}$ Nm.

The slip on the fault plane is determined relative to the hypocenter. Therefore, the location of the hypocenter used has an effect on the geographical locations of the slip patches. Furthermore, the depth can have an effect on the observed pattern of slip. In Mexico it has been noticed that hypocenters estimated from global data tend to be mislocated toward the northeast by on the order of 20 km (Hjörleifsdóttir et al., 2016; Singh & Lermo, 1985), and we therefore use the hypocentral location reported by a local network (Red Sísmica del Estado de Colima, RESCO) (lat. 18.81° N, lon. 104.54° W, and depth 17.0 km); however, we set the hypocenter depth to 20 km so that the fault plane does not reach the surface far from the trench.

Other subjective choices are the weight on each wavelet coefficient (the relative importance of different periods) and the relative weight of static, long-period, and body wave data. Here we use the wavelet coefficients typically used in the FFF algorithm (Ji et al., 2002a, 2002b). We use the same weight on body and surface waves but vary the relative importance of the static data. Furthermore, the reference rupture velocity has an important impact on the slip distribution. We will invert the data assuming both nearly fixed and variable rupture velocities.

3. Seismic Source Modeling; Results

3.1. Teleseismic Body and Surface-Wave Inversion

First, we perform an inversion of body and surface waves together. The seismograms used are chosen based on station noise level, as well as to obtain a satisfactory azimuthal coverage. We then assign the strike of the fault plane to best match the orientation of the trench, and based on initial test inversions, we select a fault plane sufficiently large as to contain all the slip in the earthquake. In this set of inversions, we do not constrain the moment, as it is well constrained by the surface-waves. We use the Crust2.0 (Bassin et al., 2000) velocity structure to describe the local structure at the source.

We inverted the observed seismograms for the slip distribution, assuming different values of nearly fixed rupture speeds $v_r = 1.5, 2.0, 2.5$, and 3.0 km/s , allowing the speed to vary locally from the average value by $\pm 0.1 \text{ km/s}$ (Figures 3a–3d). Then we performed two more inversions, with average values of $v_r = 2.0$ and 2.5 km/s , respectively, but permitting larger variations in the rupture speed of $\pm 0.8 \text{ km/s}$ (Figures 3e and 3f). All the resulting slip models have several things in common. They all rupture two patches that are more or less connected, one near the hypocenter and one to the NW, reaching up to the trench. For small values of the rupture speed, the second patch is closer to the hypocenter than for higher values of the rupture speed. Larger slip is observed over a smaller area for smaller rupture speeds and vice versa. The comparison of observed and modeled seismograms for our best fitting model ($v_r = \text{var}2.5$; Figure 3f) is shown in Figure 4.

The predicted static displacements for all models are close to or larger than the observed in the SE, near CRIP, but only about half the observed near CHAM in the NW. We note that the higher rupture velocities, $v_r = 2.0$ or 2.5 km/s , generate better matches to the static data, which was not used in the modeling.

We find that the misfit to the various data sets and constraints decreases with increasing rupture speed. This observation should be taken with caution, as increasing the rupture speed effectively allows for a larger fault plane or more free parameters. However, visibly poor fits for rupture velocity of 1.5 km/s indicates that an average rupture speed of 2 km/s or larger is required (waveforms and discussion are presented in section S1 and Figures S1–S6). Furthermore, we find that the synthetic surface waves show a larger directivity effect than observed for $v_r = 3.0 \text{ km/s}$. Allowing a variable rupture speed increases the number of free parameters further, so predictably the misfit is lower in the inversions with a larger range of allowed rupture speeds. However, we note that the slip distribution is very similar to the fixed rupture velocity model. Based on the mismatch between observed and predicted seismograms for rupture speeds of 1.5 and 3.0 km/s , we estimate an average rupture speed of $2.0\text{--}2.5 \text{ km/s}$.

However, the most notable result from these experiments is that all the models show that most of the slip occurs near the trench, with the amount of slip and size of fault patches varying only slightly with rupture speed. We performed various tests, varying the dip and the relative importance of the waveform misfit and the smoothness constraint in the inversion, and by large they show the same pattern.

3.2. Static Inversion

We invert the 11 static displacement vectors estimated by Hutton et al. (2001) and Melbourne et al. (1997) (Figure 5), using our preferred fault geometry. We find that there is little difference between the two. For each data set, we perform two inversions: (1) weight on each measurement is based on its error ($w = 1/\sigma$, where σ is the displacement uncertainty reported in each of the studies) and (2) same weight on all measurements.

The results from these inversions agree in several characteristics with the slip distributions presented by Melbourne et al. (1997) and Hutton et al. (2001). We observe most of the slip northwest from the hypocenter. We also found that the rupture is described by more than one slip patch even though we constrained the solution to be smooth. The large offsets measured at the nearest stations (CHAM, CRIP, and PURI) have the largest effect on the static solutions, as previously pointed out by Melbourne et al. (1997). The maximum slip obtained in our inversion is somewhat smaller than the results from Melbourne et al. (1997) and Hutton et al. (2001), who suggest a maximum slip of 4–5 m. However, we found that the location of the maximum slip along strike and dip are quite similar to those previously presented.

The majority of slip is located deeper and closer to the coast in this model than in the seismic models presented in the previous section. This is consistent with results of the previous studies, which suggest

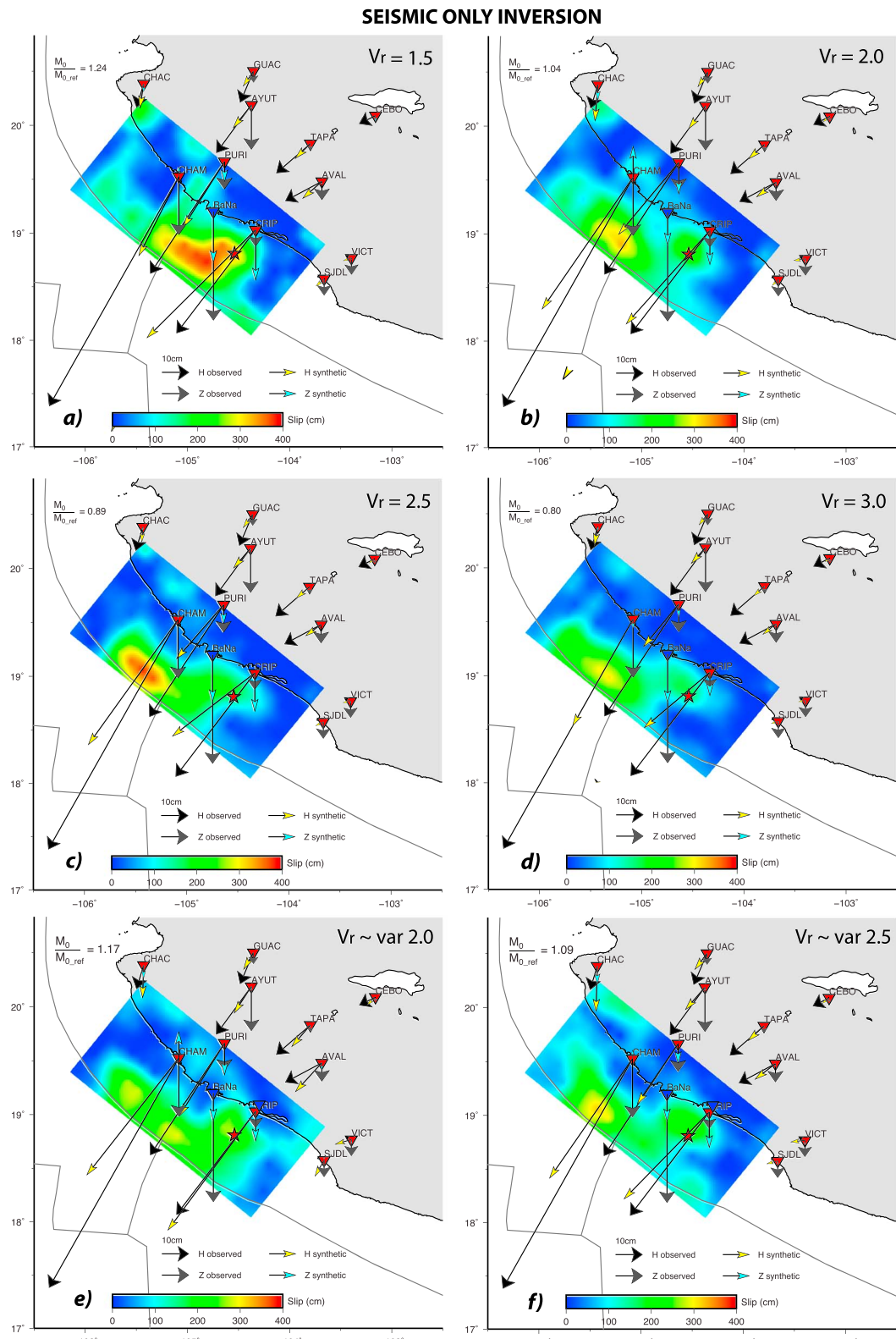


Figure 3. Slip distributions obtained from seismic data (body and surface waves). Observed horizontal and vertical displacements (Hutton et al., 2001) are shown with black and gray vectors, whereas horizontal and vertical displacements predicted by the slip model are shown with yellow and blue vectors. The slip distributions in panels (a)–(d) are obtained by fixing the rupture speed to values of 1.5, 2.0, 2.5, and 3.0 km/s. In the last two panels, the rupture speed was allowed to vary from a range of (e) 1.2–2.8 and (f) 1.7–3.2. We do not invert for the subsidence observed at the pressure sensor at Barra de Navidad (BaNa).

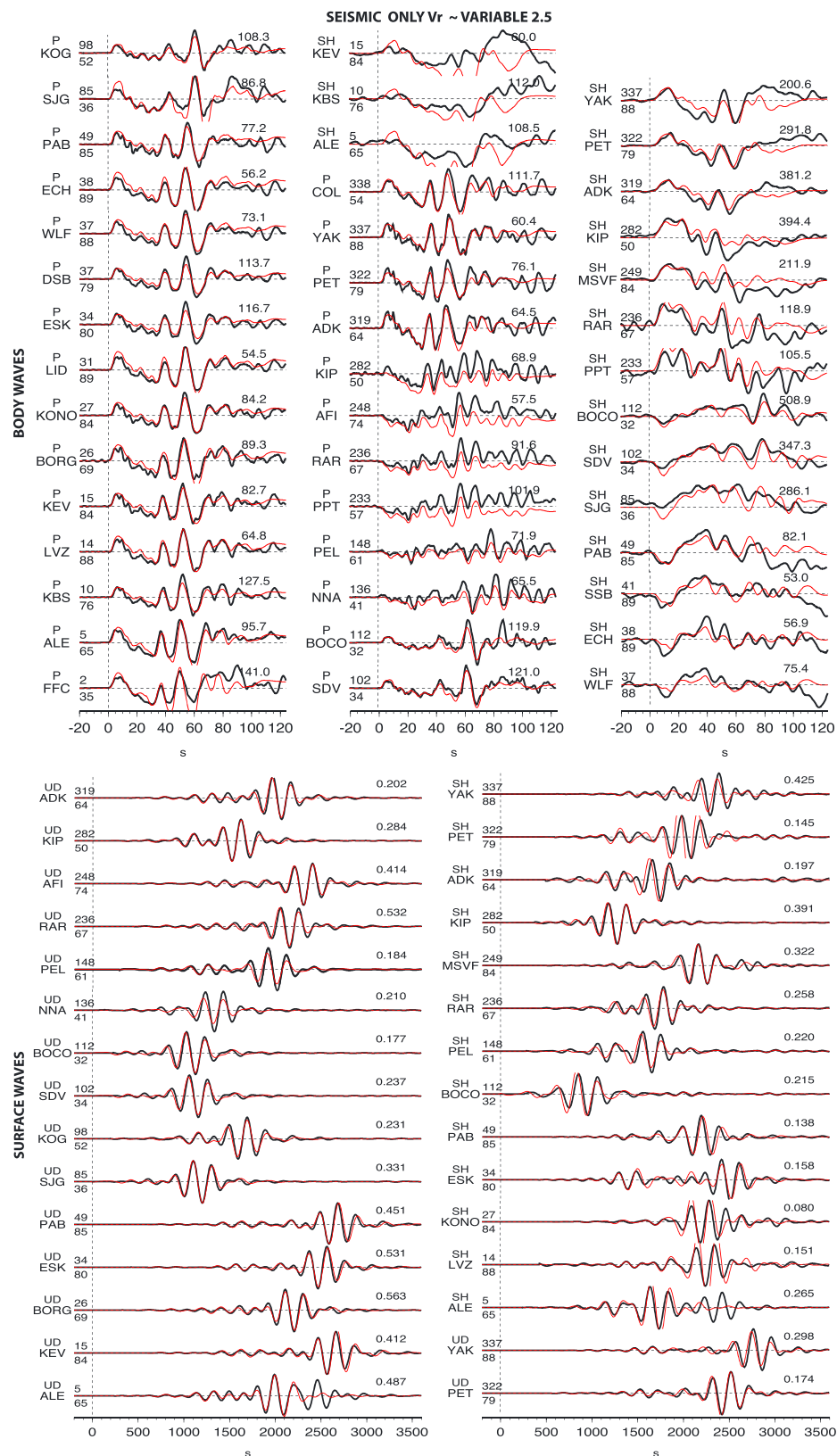


Figure 4. Observed (black) and synthetic (red) teleseismic (a) body waves, (b) surface waves for the model shown in Figure 3f. Labels on each station indicate from top to bottom, left to right. Vertical (P/UD) and transverse (SH) component, the station name, azimuth from the source, angular distance, and relative amplitude of each trace.

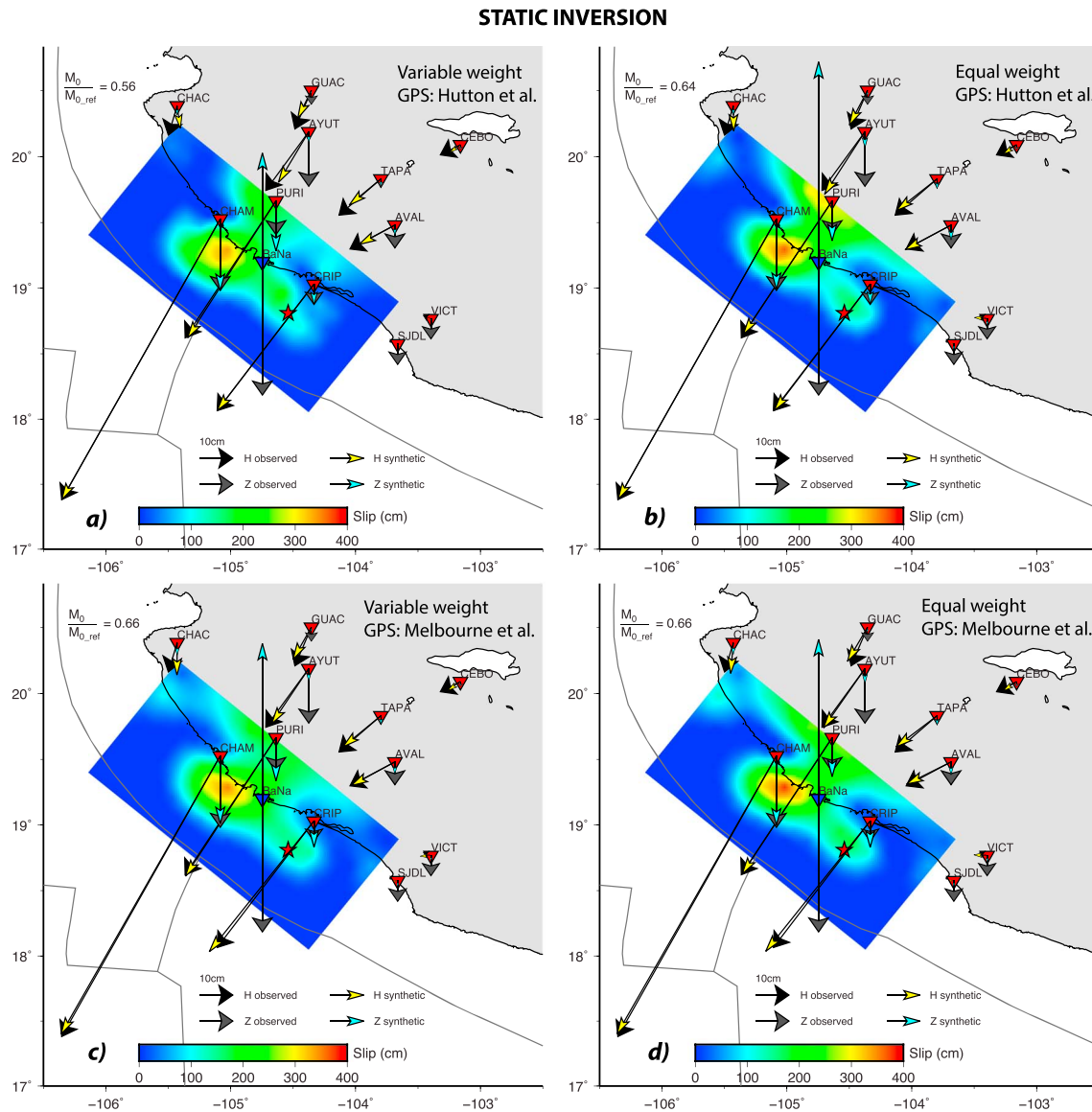


Figure 5. Slip distributions obtained from geodetic data (static offsets obtained from repeat campaign Global Positioning System measurements). Observed horizontal and vertical displacements are shown with black and gray vectors, whereas horizontal and vertical displacements predicted by the slip model are shown with yellow and blue vectors. The slip distributions in panels (a) and (b) are obtained for displacements estimated by Hutton et al. (2001) and those in panels (c) and (d) from Melbourne et al. (1997). Panels (a) and (c) have weights on the individual stations that depend on the errors, whereas for panels (b) and (d) all stations have equal weights. We do not invert for the subsidence observed at the pressure sensor at Barra de Navidad (BaNa).

that the depth of the patch may reflect the incapacity of this network to resolve slip near the trench. We performed various tests to evaluate whether the depth of the slip was an artifact of the model parameters, and how it could be reconciled with the seismic models. We tried various dips of the faults plane, different weighting of the GPS vectors relative to each other, and weighting the horizontal components more strongly relative to the vertical component. However, all of the resulting models had the majority of slip much deeper than the seismic models.

We notice an unexpected trend in the change in the vertical component as a function of distance from the trench; from PURI to AYUT and GUAC. The typical pattern would be diminishing vertical motions with distance from the end of the slip model; however, out of these three stations, we find the largest subsidence at AYUT, more than 150 km from the trench, indicating that perhaps the data at this station are erroneous. However, removing this station from the inversions does not show any significant changes in the slip pattern.

The static model predicts large uplift offshore Barra de Navidad (BaNa), contrasting with the large subsidence observed there by a moored pressure sensor. The modeled uplift/subsidence is controlled by the spatial gradient of slip below the station, or in this case the mooring. As the model predicts artificial large slip at the bottom of the fault, due to anomalously large subsidence at AYUT, the spatial gradient is small close to BaNa and large uplift is predicted. By including this site in the inversion, it is relatively easy to produce large subsidence there, simply by concentrating the slip contours near it. However, we chose not to include this station in the inversion for two main reasons: (1) It does not cover the same time period as the GPS data. (2) Strong currents due to the tsunami may have moved the mooring, in a similar way as they moved large sunken ships in the nearby lagoon (Filonov, 1997).

3.3. Joint Inversion

Finally, we invert the body waves, surface waves, and static displacements together, combining the data sets of the previous two sections. In these inversions we do not constrain the moment and we apply the same smoothing as for the seismic inversions. As one might guess from looking at the relatively different solutions in Figures 3 and 5, both data sets are not very well matched by either of the single-data set slip models. We perform several inversions, with increasing relative weights on the GPS-data set (Figure 6) compared to the seismic data. Note that the absolute weight is not meaningful; however, as we increase it from 0.001 to 1.0 the effect goes from barely considering the GPS data to requiring it to be almost exactly matched.

We find that when the weight is small on the GPS data set, the slip distributions are very similar to the seismic only models, and that the GPS vectors at the eastern section of the fault (CRIP) are well fit, whereas the displacement vector at CHAM is relatively poorly fit, especially the vertical component. Increasing the weight on the GPS data set predictably improves the match between observed and predicted static offset vectors, whereas the match to the seismic data deteriorates somewhat, when the weight rises above 0.1 (waveforms for weight of 0.1 are shown in Figure 7). Decreasing fit to the seismograms with increasing weight on the GPS data is not so easily observed by eye in the waveforms; however, the overall scalar moment increases (from $M_0/M_{0_ref} = 1.08$ for weight 0.001 on GPS to $M_0/M_{0_ref} = 1.28$ for weight 1.0 on GPS), resulting in the surface waves being on average a bit too large (section S2 and Figures S7–S12). We also see a slightly increased misfit to the first 20 s of the records at stations toward the north and northeast (for example stations FFC and LID) for a weight on GPS of 1.0. The slip models with large weight of the seismic data have large slip close to the trench, whereas the slip models with large weight on the static data have large slip near the coast, consistent with the results of previous sections. Intermediate results show relatively uniform slip between the coast and the trench.

Based on this analysis, we find that the models with weights on the static data of 0.1 or below provide predictions that can match the seismic data reasonably well, whereas weights on GPS data of 0.05 or higher give good matches to the static offsets (Figure 6). We note that there is therefore a range of models that give reasonably good matches to both data sets simultaneously.

3.4. Comparison With Previous Slip Models

Several studies have presented kinematic seismic source models of the 1995, Jalisco earthquake. Some characteristics of this earthquake appear in all the models; the rupture propagated to the north west of the hypocenter and the approximate length of the rupture was between 150 and 200 km. However, there is an important disagreement in the slip distributions obtained from the different types of data used in the analysis. Inversions for the rupture history based on inversion of broadband recordings of teleseismic body waves (Mendoza et al., 2011; Mendoza & Hartzell, 1999; Ye et al., 2016) as well as joint inversion of body and surface waves (USGS *finite fault solution*) show slip near the hypocenter followed by shallow slip, with maximum values of 3–4 m at a distance between 70 and 130 km NW of the hypocenter and at distances of 10–40 km from the trench. In contrast, the models presented by Melbourne et al. (1997) and Hutton et al. (2001) from the inversion of the available geodetic data, maximum slip values of 4–5 m were located at 55 km away from the trench in the downdip direction.

The slip models obtained when matching static and seismic data in this study are very similar to those obtained by other researchers using the corresponding data sets; the seismic slip model is similar to those presented by Mendoza and Hartzell (1999), Mendoza et al. (2011), and Ye et al. (2016) and the USGS Finite fault slip model, whereas the static slip model resembles the models by Melbourne et al. (1997) and

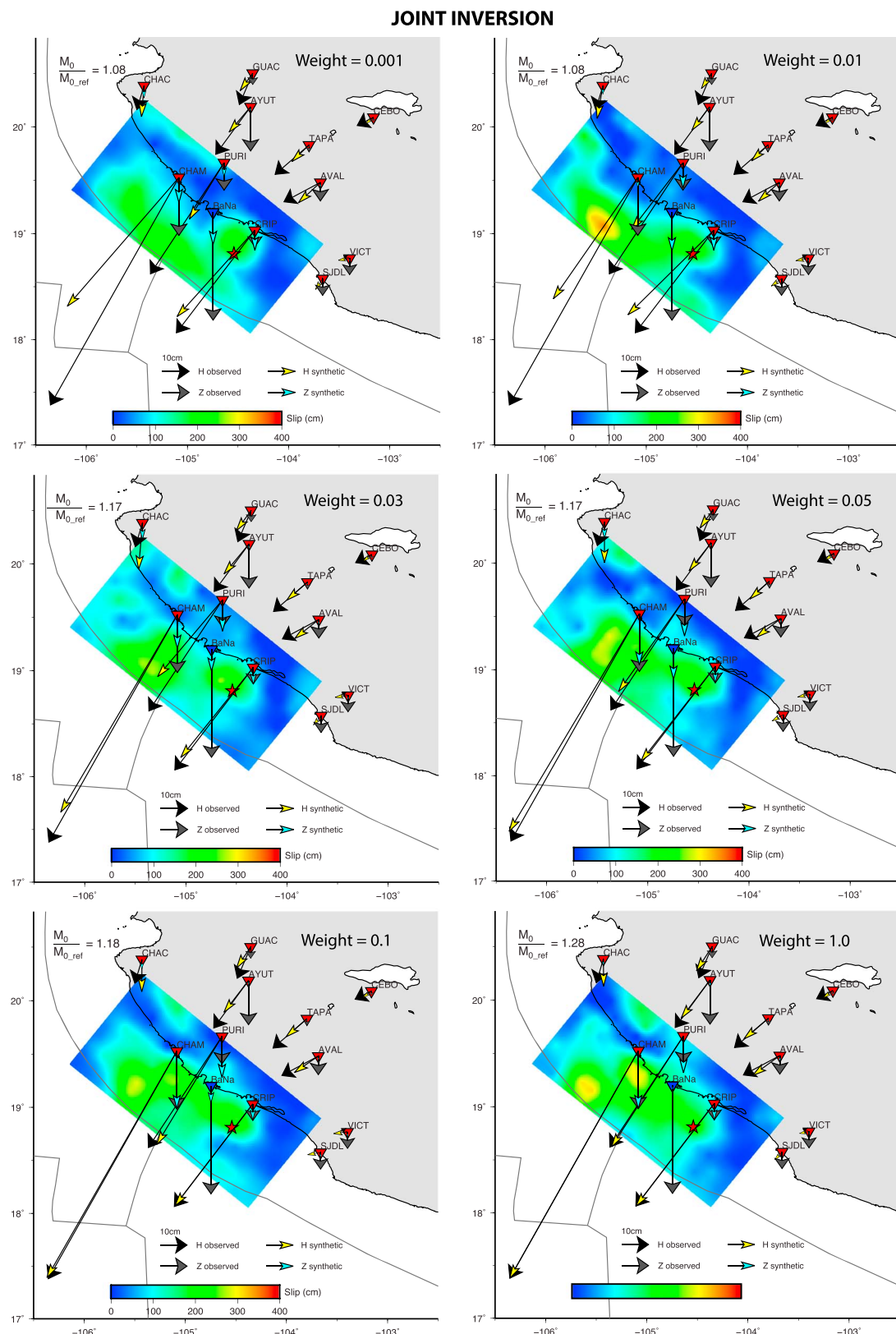


Figure 6. Slip distributions obtained from seismic (body and surface waves) together with geodetic data, displacement vectors same as in Figure 3. The panels (a) to (f) have increasing weight on the Global Positioning System data set relative to the seismic, as marked. We do not invert for the subsidence observed at the pressure sensor at Barra de Navidad (BaNa).

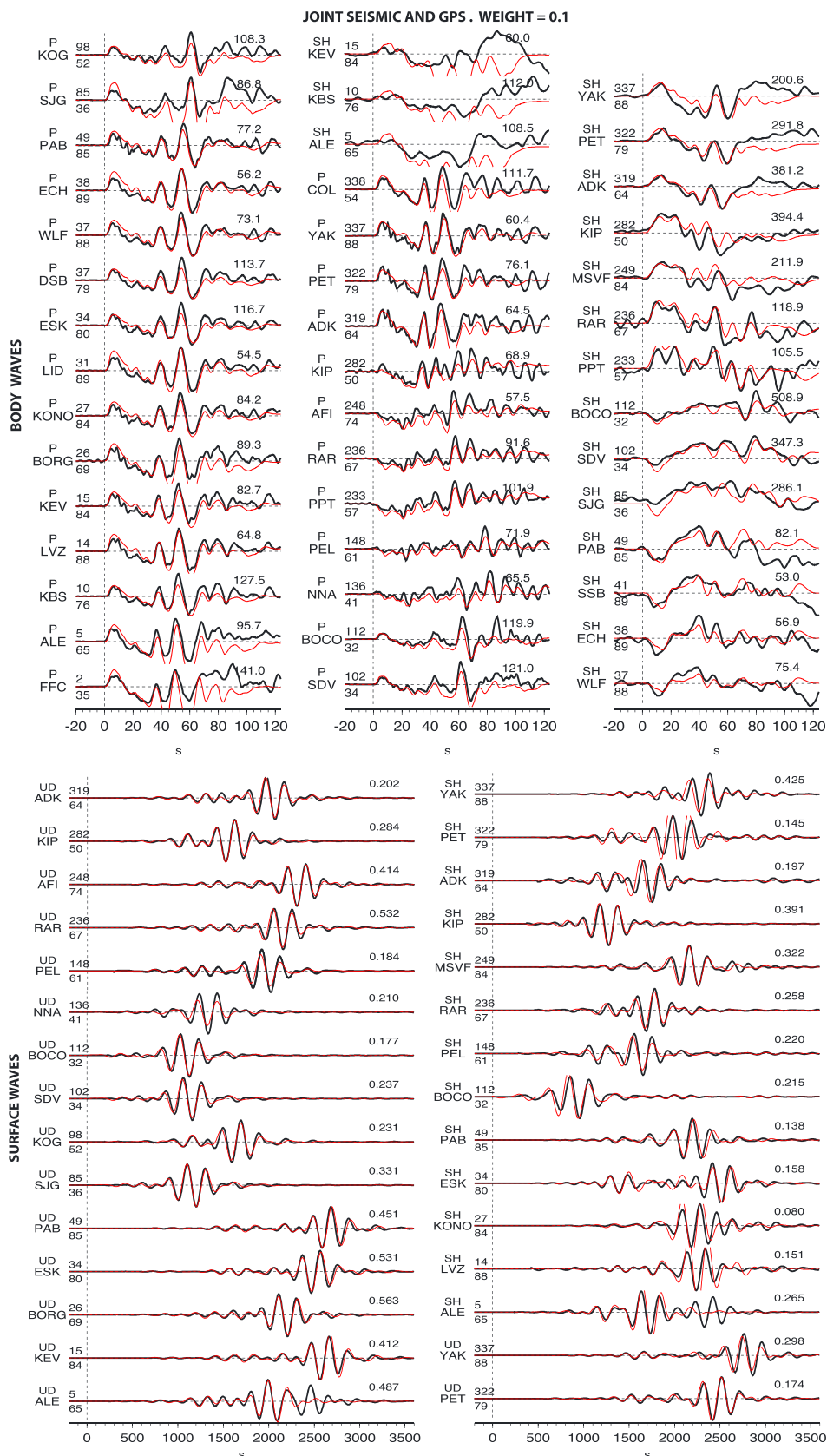


Figure 7. Teleseismic waveforms for joint seismic and geodetic slip model, with weight 0.1 (Figure 6e). Labels same as Figure 4.

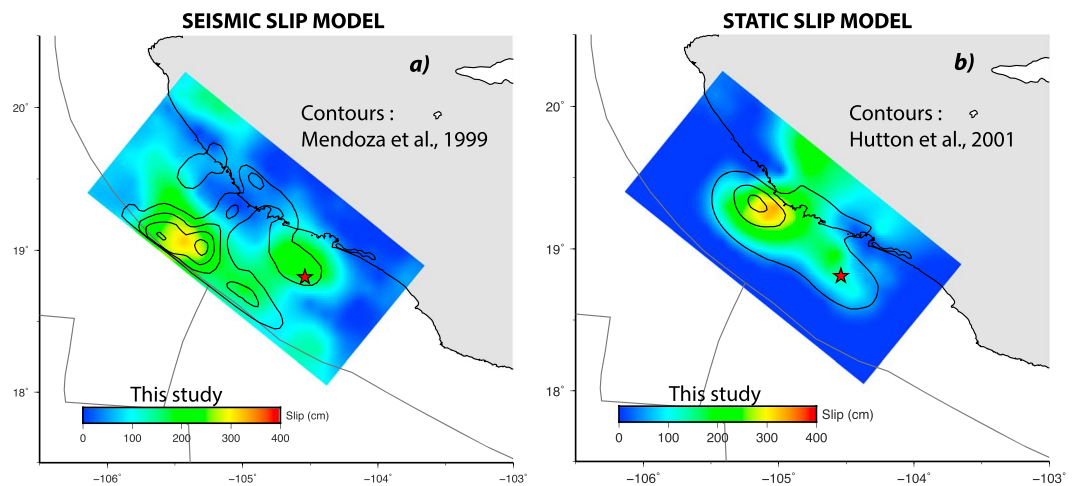


Figure 8. Comparison of slip models obtained in this study (colors) to those obtained by other researchers (contours). (a) Our seismic only model (variable rupture velocity, $v_r = 1.9\text{--}3.1$), versus the seismic only model of Mendoza et al. (1999), contour lines every 0.5 m. (b) Comparison of our geodetic only model, to the geodetic only model by Hutton et al. (2001), contour lines every 1 m.

Hutton et al. (2001) obtained using the same data set (Figure 8). On one hand these results are reassuring, as using the same data leads to similar models, regardless of the details of the methods used. On the other hand the differences between the static and seismic models are disconcerting, as there can only be one true coseismic slip model.

4. Discussion

4.1. Alternative Model: Afterslip

There are several indications that the 1995 Jalisco event produced small high-frequency radiation compared to other earthquakes: (1) ratios of total radiation to high-frequency radiation in Mexico City (at about 500 km distance) are high compared to other Mexican earthquakes and similar to ratios of events that are located near the trench (Shapiro et al., 1998); (2) estimated energy-to-moment ratio, $E_S/M_0 = 4.2\text{e}{-}6$, is smaller than the ratios for other subduction zone events nearby (Pérez-Campos et al., 2003; Pérez-Campos & Beroza, 2001), and similar to that of tsunami earthquakes (Ye et al., 2016); (3) moreover, the 9 October 1995 earthquake exhibited the largest disparity along the Mexican Subduction Zone between the estimated M_S (7.4) and the M_W (8.0) (Pacheco et al., 1997).

The small high-frequency radiation by this event has grouped it together with tsunami or near-trench earthquakes. However, the joint model, presented in the previous section, breaks (at least almost) all the way to the coast, making this event only partially a *near-trench* event.

We will now show that there is an alternative model. Perhaps one of the most critical assumptions we have made up to this point is that the measured static displacement vectors include only the coseismic displacements and that no other slip occurred during the rest of the measurement period. However, rapid afterslip following this earthquake has been suggested, based on the daily averages of the tidal record in Manzanillo (a few kilometers northeast of GPS station CRIP), compared to tidal records in Acapulco and Puerto Vallarta. This comparison shows a coseismic subsidence of 14 cm in Manzanillo, contrasting with 7 ± 2 cm of uplift in the following 4 days (Melbourne et al., 2002). Given that the static offsets used in this study were measured 5–10 days after the event, this type of large early afterslip could significantly influence them.

We therefore hypothesize that there was a significant contribution to the measured geodetic offsets from aseismic slip and further assume that the coseismic slip is well described by the seismic only models. As the tide gauge records suggest large afterslip, we will assume that the aseismic slip occurs after the event, although we cannot exclude that a significant part of it occurs in a slow-slip event in the 6 months before

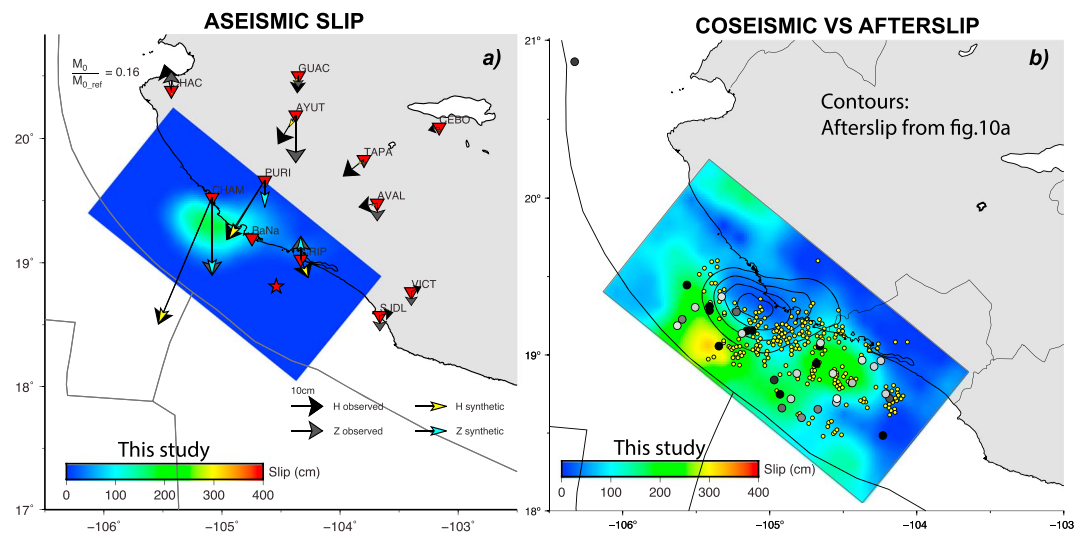


Figure 9. Modeling the displacements not predicted by the seismic only model. (a) The black vectors show residual between the observed displacements (Hutton et al., 2001) and those predicted by our preferred seismic only model (variable rupture velocity, $v_r = 1.9\text{--}3.1$). The slip model shown is that which best predicts the differences, and the colored vectors are the displacements predicted by this model. (b) Our preferred seismic model shown with colors, overlaid with the contours (every 0.5 m) of the slip model shown in Figure 9a, together with aftershock locations from a local network (small yellow circles, Pacheco et al., 1997), as well as corrected aftershock locations (see text) from global networks (larger circles). Timing of aftershocks is shown with progression from white (first day after earthquake) to black (5 days after earthquake and later) circles.

the earthquake. Furthermore, we do not consider the possibility of viscoelastic rebound causing postseismic motion, due to the short timescales involved. We can then pose the question of how much afterslip is required to match the difference between the predicted offsets for the seismic only model and the observed static offsets.

Next we assume that the difference in the seismic and geodetic models is due to afterslip. We can then estimate the static deformation due to the aseismic slip by subtracting the contribution of the coseismic slip, as predicted by our best coseismic model, from the observed static displacements. We use the coseismic slip model with a variable rupture velocity, centered on 2.5 km/s (Figure 3f). We now invert for the slip distribution of the aseismic event that best predicts the residual static deformation (Figure 9a). We find highly localized slip of up to 1.8 meters offshore station CHAM, with slip above 1 m in an elliptical area of about 40×60 km. Comparing the slip in the aseismic event to that during the seismic event (Figure 9b), we see that the aseismic slip has little overlap with the coseismic slip and is nested in the corner downdip of the shallower asperity and northwest of the deeper asperity of the coseismic slip distribution. It should be emphasized that the details of the slip distribution of the aseismic slip depends heavily on the coseismic slip model chosen for the modeling. However, all of the seismic only models show a large underestimate of the static offset of GPS station CHAM, indicating that most of the aseismic slip would have to occur near that station.

Interestingly, the seismic only models predict larger subsidence at CRIP (13.3 cm) than observed by the GPS station 6 days after the earthquake (6.2 cm; Hutton et al., 2001; Figure 3f), leading to a positive residual (7.1 cm), which requires uplift in the postseismic period. These predictions are consistent with observed tide gauge records (Melbourne et al., 2002), which suggest 14.2 ± 2 cm subsidence during the earthquake and a gradual uplift of 7 ± 2 cm during the following 6 days. We note that the close agreement between the subsidence and subsequent uplift predicted by our analysis and the tide gauge may be a coincidence, as both estimates have large errors. The subsidence values predicted by our modeling depend heavily on the choice of coseismic model and those estimated by the tide gauge measure the difference in sea level between two stations, which may depend on other factors than just the ground deformation, such as sea condition. However, we conclude that their overall agreement supports the general pattern of our model.

We find that the aftershocks located by a regional network (Pacheco et al., 1997) are concentrated in the area between the maximums of the coseismic and afterslip (Figure 9b). Unfortunately, the timing information of these aftershocks has been lost. Locations of earthquake in this part of the Mesoamerican subduction zone by global networks are biased on average by 21 km toward 62° (Hjörleifsdóttir et al., 2016; Singh & Lermo, 1985), but correcting for that bias, we can get an approximate location of the largest aftershocks from global networks (Figure 9b). Of the 35 aftershocks reported by NEIC during the first month after the earthquake, 7 of them occur within the first day after the earthquake and 23 within 5 days of the event. We do not see a time progression in the location of the aftershocks within this time period.

The afterslip inferred in this study is very rapid and large. The maximum afterslip (~1.8 m) within 5–10 days of the event is about half the maximum coseismic slip (~3.5 m). However, the scalar moment of the afterslip in the first 5–10 days is only 16% of the coseismic moment. Similar rapid afterslip in the first day has been seen after other events: 20% of coseismic displacements in first day after the M_w 6.3, 2009, L'Aquila, Italy, earthquake (Yano et al., 2014); 7% in the first 3 hr after the M_w 7.6, 2012, Nicoya, Costa Rica, earthquake (Malservisi et al., 2015); and 30% in the first 24 hr after both the M_w 7.6 1994 Sanriku-Haruka-Oki, Japan, earthquake (Heki and Tamura, 1997) and the M_w 7.8, 2010, Mentawai, Indonesia event (Hill et al., 2012). Furthermore, large afterslip to coseismic slip ratios have been observed for several other earthquakes in the Middle America Trench, such as the Pinotepa-Nacional/Ometepec M_w 7.5 earthquake in 2012 (Graham et al., 2014), the M_w 7.2, 2012, El Salvador earthquake, and the M_w 6.9, 2004, 9 October, Nicaragua earthquake (Geirsson et al., 2015).

It has been suggested that large afterslip relative to coseismic slip may be characteristic of tsunami type events, weakly coupled regions, as well as regions on the boundary between fault areas with velocity strengthening and weakening friction (Geirsson et al., 2015). This would suggest a transition from a more highly coupled region in the southeastern part of the fault plane slipping in the 1995 Jalisco event, to a fault patch with smaller coupling or conditionally stable creep in the northwestern part of the fault plane.

4.2. Tsunami Modeling

In previous sections, we have obtained substantially different slip models that can predict observed seismic and/or static displacements. Some models show large slip near the trench, and others near the coast. These models could be expected to generate very different tsunamis. In order to test whether we can use the tsunami observations to distinguish between the different models, we carried out simulations for three representative slip models based on the joint inversions: (a) adjusted to fit principally the seismic data (weight on GPS 0.001; Figure 3a), (b) joint model (weight on GPS 0.1; Figure 3e), and (c) adjusted to fit mostly the GPS data (weight on GPS 1; Figure 3f). The tsunami numerical simulations were carried out with GeoClaw, a validated tsunami propagation model that solves the nonlinear shallow water equations (LeVeque et al., 2011). A table of observed runup and details of the methodology used to calculate the tsunami wave height and propagation are presented in Table S1 and section S2 (Becker et al., 2009; Borrero et al., 1997; Carrillo-Martinez, 1997; Černý et al., 2016; Geist, 1998, 2002; Jarvis et al., 2008; Lander et al., 2003; Ramírez-Herrera et al., 2016; Synolakis, 1991). Snapshots of the predicted wave height at 9 min after the earthquake initiation time show that the crest of the seismic only model (model a) is higher but has not arrived at the coast at this time. On the other hand, the joint (model b) and static-only model (model c) has wider crests that have already arrived at the coast at this time (Figures 10a–10c). Looking at other time frames, we find that the simulated arrival time for the first waves vary between 10 and 20 min, consistent with the reported times (Filonov, 1997). We also note that in the region between Chola, Jalisco to Caleta de Campos, Michoacán (between 75 and 100 km along the trench), the seismic model predicts larger wave heights than the static model, whereas the joint inversion predicts an intermediate value. All three models show peaks of local amplification at two locations along the coast that are not related to the arrival of the first wave, with the maximum amplitude occurring more than 40 min after the first arrival.

A similar observation can be made by comparing the modeled tsunami waveforms with pressure recorded by a conductivity-temperature-depth mooring deployed at 30-m depth offshore Barra de Navidad (Ortiz et al., 2000). We find that the timing of the first arrivals for the seismic only and joint models (models a and b) are later than observed, whereas the first arrival for the static only model (model c) are slightly earlier. The amplitude of the waveforms cannot be directly compared, as the pressure sensor is not moored at the bottom but at 20 m above the seafloor, which induces pendular movements as the mooring moves horizontally

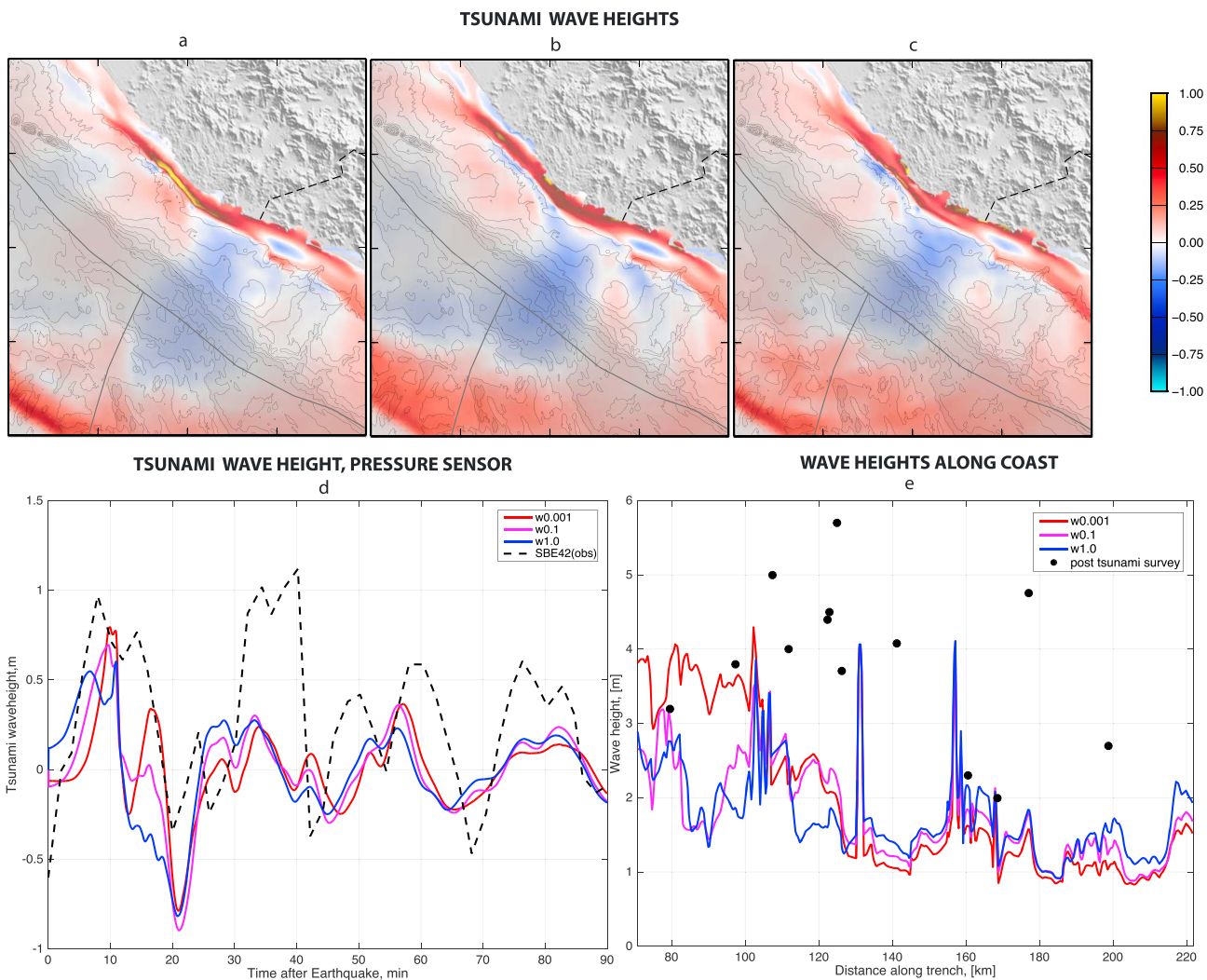


Figure 10. Predicted tsunami wave height 9 min after earthquake for three different models: (a) Seismic (w0.001). (b) Joint Seismic and GPS (w0.1). (c) GPS (w1.0). (d) Corresponding estimated waveforms compared to the conductivity-temperature-depth mooring/pressure sensor offshore Barra de Navidad (amplitude scaled by 0.5). (e) Calculated tsunami wave heights along the coast compared to the posttsunami survey observations.

and down with the tsunami waves, inducing additional pressure. We have scaled the observed waveform by 0.5 for comparison. The maximum difference in the arrival time of the first tsunami wave between models is on the order of 5 min.

We find that only few of the runup observations show a fair agreement with the tsunami simulations (Figure 10e). In particular, the middle section of the domain does not have a good agreement between observed and simulation. This is consistent with recent work by Mori et al. (2017), who model the tsunami produced by a seismic only slip model for this event and find that the predicted tsunami is much smaller than observed. The morphology of the Manzanillo area is relatively complex as it has several bays that are known to be prone to resonance effects (see for example Okal & Synolakis, 2015). The largest observed runup occurs in one of the bays of the Manzanillo region, consistent with our simulations. Furthermore, most of the measurements are made in bays, where the waves can amplify, possibly biasing the observations to larger values. Unfortunately, the resolution of the available bathymetry data limits the possibility of proper simulations including runup and inundation areas. This could be resolved by future work that includes higher resolution bathymetry and topography, allowing for more accurate simulations. We therefore conclude that we are not able to use the tsunami modeling to distinguish between the end-member scenarios.

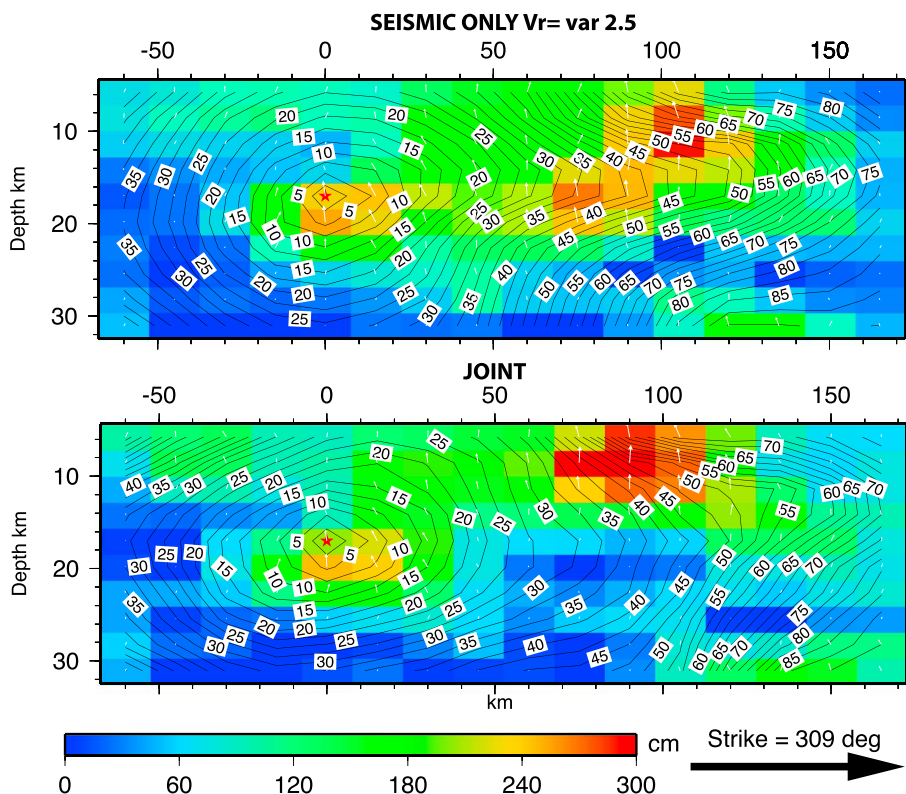


Figure 11. Slip on fault for the best fit seismic only model (Figure 3f) and for the joint model with weight 0.1 (Figure 6e). Slip amplitude is shown with colors, direction with white arrows, and timing of rupture at each point with black rupture contours. The contours are very dense in the large slip or red patch, suggestive of a slower rupture velocity.

4.3. Relatively High Average Rupture Speed

Typically, earthquakes that break the near-trench area have slow rupture speeds, which can be as low as 1.0 km/s (Ammon et al., 2006; Kanamori & Kikuchi, 1993). On the contrary, the 1995 event had an average rupture speed of 2–2.5 km/s, which is typical for subduction zone earthquakes at traditionally seismogenic depths. This is a relatively robust result, as models with average rupture speeds of as high as 1.5 km/s generate substantially poorer fits to the observed seismograms than the more rapid ones. This may be explained in at least two ways: (1) the shallow fault plane properties in the Jalisco area are more similar to those at greater depth than in other subduction zones and (2) the earthquake ruptured both the shallow and the deeper part, as suggested by the joint models that have similar relative weights on the seismic and static observations (Figure 6c and 6d) and the average speed is a combination of a faster rupture at depth and a slower rupture near the trench. Analyzing the rupture contours for the inversions where variable rupture speed was allowed, we find that indeed the rupture speed in the shallow large-slip patches is as low as 1–1.5 km/s for both the seismic only and joint solutions (Figure 11), consistent with the second explanation above. However, the variations in rupture speed along the fault plane are not well resolved, and although this finding is suggestive, it is not robust. Furthermore, we cannot resolve systematic variations in the risetime along the rupture plane.

4.4. Recurrence Times

The M_w 8.0 1995 Jalisco event, together with the M_w 8.2 1932 Jalisco and M_w 8.0 1985 Michoacán earthquakes, is the three largest events to break the Mexican subduction interface in the last 100 years. It is somewhat surprising that two of these events break the same segment of the subduction zone. When should we expect the next event in this segment? The answer to this question depends on whether there was significant overlap between the rupture areas in the two events or not. Based on high seismic intensities, it has been suggested that the 1932 earthquake broke the fault surface near the coast (Singh et al., 1985).

Comparing the slip in the 1995 earthquake, of about 2 m over a large part of the rupture area (although reaching 3.5 m in the large slip patches), to the convergence rate between the Rivera and the North American plate, of about 3.3 cm/year (DeMets et al., 2010) or increasing from 3.9–4.8 cm/year going southeast along the rupture (Bandy, 1992; Kostoglodov & Bandy, 1995), and supposing that the plates are fully coupled, we would expect this type of event every 45–60 years or so.

The recurrence interval of the 1932 3 June event, supposing it had a coseismic slip of 3–5 m (somewhat larger than the 1995 event) and that there was little spatial overlap between that and the 1995 events may be on the order of 100–200 years. This recurrence interval suggests that we could expect another 1932 Jalisco earthquake in the next 100 years, with possibly severe consequences for this now much more populated area. However, the two end-member scenarios have slip (either coseismic or seismic) close to the cost, suggesting a possible overlap between the 1932 and 1995 rupture. This would indicate that the some of the accumulated slip deficit was released in this event, which may delay the next event in this segment.

5. Conclusions

We invert for the slip during the 1995 M_w 8.0 Jalisco, Mexico, earthquake, using seismic and geodetic (campaign GPS) data. We find that the slip distribution depends heavily on the data set used, slip in a deeper patch near the hypocenter and in a shallower patch toward the trench when using seismic data and slip in two patches close to the coast when using geodetic data. These results are very similar to those of other authors using the same data sets. Joint inversions of both data sets simultaneously show relatively uniform slip between the coast and the trench. The 1995 earthquake has macroseismic properties, such as the ratio between radiated energy to moment, typical for tsunami or near-trench earthquakes. However, although the joint inversion shows larger slip close to the trench than typical for Mexican earthquakes, there is substantial slip deep into the zone typically considered seismogenic. This is atypical for earthquakes with macroseismic properties similar to those of tsunami earthquakes.

Alternatively, we obtain a different model by allowing for rapid postseismic slip affecting the observed static offsets. With this assumption we find that more than 1 m of aseismic slip occurs in an elliptical area of about 40×60 km, most likely as afterslip during the 5–10 days after the earthquake. The afterslip fits into a gap in the coseismic slip model, downdip of the shallower slip patch, and to the northwest of the deeper slip patch. Most of the aftershocks occur on the boundary between the coseismic and aseismic slip areas. Slow-slip events have been observed in the same region as the afterslip reported in this study. The aseismic slip could significantly increase the expected recurrence interval of earthquakes in this zone.

We model the tsunami resulting from three representative models, but we were not able to discriminate between them based on the comparison of observed and modeled tsunami wave height. We find that the average rupture speed (2–2.5 km/s) is more similar to that of typical subduction earthquakes than the tsunami earthquakes that often break the near-trench area, although this average may be a combination of a faster rupture at depth and a slower shallower rupture speed.

The assumptions that there is no postseismic motion (joint inversion) or that all the difference between seismic and geodetic models are due to postseismic motions can be seen as two permissible end-member models. It is plausible that the true model is somewhere in between these two scenarios and that the Jalisco earthquake was only partially a *near-trench* earthquake.

References

- Abe, K. (1981). Magnitudes of large shallow earthquakes from 1904 to 1980. *Physics of the Earth and Planetary Interiors*, 27(1), 72–92. [https://doi.org/10.1016/0031-9201\(81\)90088-1](https://doi.org/10.1016/0031-9201(81)90088-1)
- Ammon, C., Lay, T., Kanamori, H., & Cleveland, M. (2011). A rupture model of the 2011 off the Pacific coast of Tohoku earthquake. *Earth, Planets and Space*, 63(7), 693–696. <https://doi.org/10.5047/eps.2011.05.015>
- Ammon, C. J., Kanamori, H., Lay, T., & Velasco, A. A. (2006). The 17 July 2006 Java tsunami earthquake. *Geophysical Research Letters*, 33, L24308. <https://doi.org/10.1029/2006GL028005>
- Anderson, J., Singh, S., Espindola, J. M., & Yamamoto, J. (1989). Seismic strain release in the Mexican subduction thrust. *Physics of the Earth and Planetary Interiors*, 58(4), 307–322. [https://doi.org/10.1016/0031-9201\(89\)90102-7](https://doi.org/10.1016/0031-9201(89)90102-7)
- Bandy, W. (1992). *Geological and geophysical investigation of the Rivera-Cocos plate boundary: Implications for plate fragmentation*. Mexico City, Mexico: Universidad Nacional Autónoma de Mexico.

Acknowledgments

We thank Ryota Hino for helpful discussions. All data used in this paper have either been previously published or are publicly available. Seismograms were obtained from the open access database of the Incorporated Research Institutions for Seismology (IRIS), networks II, IU, and G, and geodetic and tsunami data from published literature as explained in text. Graphics were prepared using the Generic Mapping Tools (GMT, Wessel, and Smith). Hjörleifsdóttir thanks UNAM/DGAPA/PAPIIT grants IB101812 and IN111316, Ramírez-Herrera thanks PASPA-DGAPA-2015 and SEP-CONACYT grant 129456. Castillo-Aja thanks for CONACYT PhD scholarship. Slip models can be accessed on the finite-source rupture model database (SRCMOD).

- Bassin, C., Laske, G., & Masters, G. (2000). The current limits of resolution for surface wave tomography in North America. *Eos, Transactions American Geophysical Union*, 81(48), F897.
- Becker, J. J., Sandwell, D. T., Smith, W., Braud, J., Binder, B., Depner, J., et al. (2009). Global bathymetry and elevation data at 30 arc seconds resolution: SRTM30_PLUS. *Marine Geodesy*, 32(4), 355–371. <https://doi.org/10.1080/01490410903297766>
- Bird, P. (2003). An updated digital model of plate boundaries. *Geochemistry, Geophysics, Geosystems*, 4(3), 1027. <https://doi.org/10.1029/2001GC000252>
- Borroto, J., Ortiz, M., Titov, V., & Synolakis, C. (1997). Field survey of Mexican tsunami produces new data, unusual photos. *Eos, Transactions American Geophysical Union*, 78(8), 85–88. <https://doi.org/10.1029/97EO00054>
- Byrne, D., Davis, D., & Sykes, L. (1988). Loci and maximum size of thrust earthquakes and the mechanics of the shallow region of subduction zones. *Tectonics*, 7(4), 833–857. <https://doi.org/10.1029/TC007i004p00833>
- Carrillo-Martinez, M. (1997). Isostasis Locales del Sismo de Manzanillo del 9 de Octubre de 1995, 9:36 a.m., Estados de Colima y Jalisco, Mexico. *Revista Mexicana de Ciencias Geologicas*, 14(1), 110–113.
- Černý, J., Ramírez-Herrera, M.-T., Bógallo, M.-F., Goguitchaichvili, A., Castillo-Aja, R., Morales, J., et al. (2016). Magnetic record of extreme marine inundation events at Las Salinas site, Jalisco, Mexican Pacific coast. *International Geology Review*, 58(3), 342–357. <https://doi.org/10.1080/00206814.2015.1075230>
- DeMets, C., Gordon, R., & Argus, D. (2010). Geologically current plate motions. *Geophysical Journal International*, 181(1), 1–80. <https://doi.org/10.1111/j.1365-246x.2009.04491.x>
- Filonov, A. (1997). Researchers study tsunami generated by Mexican earthquake. *Eos*, 78(3), 21–25. <https://doi.org/10.1029/97EO00014>
- Geirsson, H., LaFemina, P., DeMets, C., Hernandez, D., Mattioli, G., Rogers, R., et al. (2015). The 2012 August 27 Mw 7.3 El Salvador earthquake: Expression of weak coupling on the Middle America subduction zone. *Geophysical Journal International*, 202(3), 1677–1689. <https://doi.org/10.1093/gji/ggv244>
- Geist, E. (1998). Local tsunamis and earthquake source parameters. *Advances in Geophysics*, 39, 117–209. [https://doi.org/10.1016/S0065-2687\(08\)60276-9](https://doi.org/10.1016/S0065-2687(08)60276-9)
- Geist, E. (2002). Complex earthquake rupture and local tsunamis. *Journal of Geophysical Research*, 107(B5), 2086. <https://doi.org/10.1029/2000JB000139>
- Graham, S. E., DeMets, C., Cabral-Cano, E., Kostoglodov, V., Walpersdorf, A., Cotte, N., et al. (2014). GPS constraints on the 2011–2012 Oaxaca slow slip event that preceded the 2012 March 20 Ometepec earthquake, southern Mexico. *Geophysical Journal International*, 197(3), 1593–1607. <https://doi.org/10.1093/gji/ggu019>
- Hayes, G. P., Wald, D. J., & Johnson, R. L. (2012). Slab1.0: A three-dimensional model of global subduction zone geometries. *Journal of Geophysical Research*, 117, B01302. <https://doi.org/10.1029/2011JB008524>
- Heki, K., & Tamura, Y. (1997). Short term afterslip in the 1994 Sanriku-Haruka-Oki earthquake. *Geophysical Research Letters*, 24(24), 3285–3288.
- Hill, E. M., Borrero, J. C., Huang, Z., Qiu, Q., Banerjee, P., Natawidjaja, D. H., et al. (2012). The 2010 Mw 7.8 Mentawai earthquake: Very shallow source of a rare tsunami earthquake determined from tsunami field survey and near-field GPS data. *Journal of Geophysical Research*, 117, B06402. <https://doi.org/10.1029/2012JB009159>
- Hjörleifsdóttir, V., Singh, S., & Husker, A. (2016). Differences in epicentral location of Mexican earthquakes between local and global catalogs: An update. *Geofísica Internacional*, 55(1), 79–93.
- Hutton, W., DeMets, C., Sánchez, O., Suárez, G., & Stock, J. (2001). Slip kinematics and dynamics during and after the 1995 October 9 Mw = 8.0 Colima-Jalisco earthquake, Mexico, from GPS geodetic constraints. *Geophysical Journal International*, 146(3), 637–658. <https://doi.org/10.1046/j.1365-246X.2001.00472.x>
- Ito, Y., Hino, R., Suzuki, S., & Kaneda, Y. (2015). Episodic tremor and slip near the Japan Trench prior to the 2011 Tohoku-Oki earthquake. *Geophysical Research Letters*, 42, 1725–1731. <https://doi.org/10.1002/2014gl062986>
- Ito, Y., Tsuji, T., Osada, Y., Kido, M., Inazu, D., Hayashi, Y., et al. (2011). Frontal wedge deformation near the source region of the 2011 Tohoku-Oki earthquake. *Geophysical Research Letters*, 38, L00G05. <https://doi.org/10.1029/2011gl048355>
- Jarvis, A., Reuter, H. I., Nelson, A., and Guevara, E. (2008). Hole-filled SRTM for the globe version 4. Available from the CGIAR-CSI SRTM 90m Database,
- Ji, C., Helmberger, D. V., Wald, D. J., & Ma, K. (2003). Slip history and dynamic implications of the 1999 Chi-Chi, Taiwan, earthquake. *Journal of Geophysical Research*, 108(B9), 2412. <https://doi.org/10.1029/2002jb001764>
- Ji, C., Wald, D., & Helmberger, D. (2002a). Source description of the 1999 Hector Mine, California, earthquake. Part I: Wavelet domain inversion theory and resolution analysis. *Bulletin of the Seismological Society of America*, 92(4), 1192–1207. <https://doi.org/10.1785/0120000916>
- Ji, C., Wald, D. J., & Helmberger, D. V. (2002b). Source description of the 1999 Hector Mine, California, earthquake. Part II: Complexity of slip history. *Bulletin of the Seismological Society of America*, 92(4), 1208–1226. <https://doi.org/10.1785/0120000917>
- Kanamori, H. (1972). Mechanism of tsunami earthquakes. *Physics of the Earth and Planetary Interiors*, 6(5), 346–359. [https://doi.org/10.1016/0031-9201\(72\)90058-1](https://doi.org/10.1016/0031-9201(72)90058-1)
- Kanamori, H., & Kikuchi, M. (1993). The 1992 Nicaragua earthquake: A slow tsunami earthquake associated with subducted sediments. *Nature*, 361(6414), 714–716. <https://doi.org/10.1038/361714a0>
- Kostoglodov, V., & Bandy, W. (1995). Seismotectonic constraints on the convergence rate between the Rivera and North American plates. *Journal of Geophysical Research*, 100(B9), 17977–17989. <https://doi.org/10.1029/95JB01484>
- Lander, J. F., Whiteside, L. S., & Lockridge, P. A. (2003). Two decades of global tsunamis 1982–2002. *Science of Tsunami Hazards*, 21(1), 1–88.
- Lay, T., Kanamori, H., Ammon, C. J., Koper, K. D., Hutko, A. R., Ye, L., et al. (2012). Depth-varying rupture properties of subduction zone megathrust faults. *Journal of Geophysical Research*, 117, B04311. <https://doi.org/10.1029/2011JB009133>
- LeVeque, R., George, D., & Berger, M. (2011). Tsunami modelling with adaptively refined finite volume methods. *Acta Numerica*, 20, 211–289. <https://doi.org/10.1017/S0962492911000043>
- Malservisi, R., Schwartz, S. Y., Voss, N., Protti, M., Gonzalez, V., Dixon, T. H., et al. (2015). Multiscale postseismic behavior on a megathrust: The 2012 Nicoya earthquake, Costa Rica. *Geochemistry, Geophysics, Geosystems*, 16, 1848–1864. <https://doi.org/10.1002/2015GC005794>
- Melbourne, T., Carmichael, I., DeMets, C., Hudnut, K., Sanchez, O., Stock, J., et al. (1997). The geodetic signature of the M8.0 Oct. 9, 1995, Jalisco Subduction earthquake. *Geophysical Research Letters*, 24(6), 715–718. <https://doi.org/10.1029/97GL00370>
- Melbourne, T. I., Webb, F. H., Stock, J. M., & Reigber, C. (2002). Rapid postseismic transients in subduction zones from continuous GPS. *Journal of Geophysical Research*, 107(B10), 2241. <https://doi.org/10.1029/2001JB000555>
- Mendoza, C., & Hartzell, S. (1999). Fault-slip distribution of the 1995 Colima-Jalisco, Mexico, earthquake. *Bulletin of the Seismological Society of America*, 89(15), 2857–2860. <https://doi.org/10.1029/98GL02059>

- Mendoza, C., Torres, C., & Gonzalez, G. (2011). Moment-constrained finite-fault analysis using teleseismic P waves: Mexico Subduction Zone. *Bulletin of the Seismological Society of America*, 101(6), 2675–2684. <https://doi.org/10.1785/0120100126>
- Mori, N., Muhammad, A., Goda, K., Yasuda, T., & Ruiz-Angulo, A. (2017). Probabilistic tsunami hazard analysis of the pacific coast of Mexico: Case study based on the 1995 Colima earthquake tsunami. *Frontiers in Built Environment*, 3, 34.
- Newman, A., Hayes, G., Wei, Y., & Convers, J. (2011). The 25 October 2010 Mentawai tsunami earthquake, from real-time discriminants, finite-fault rupture, and tsunami excitation. *Geophysical Research Letters*, 38, L05302. <https://doi.org/10.1029/2010GL046498>
- Okada, T., Yaginuma, T., Umino, N., Kono, T., Matsuzawa, T., Kita, S., & Hasegawa, A. (2005). The 2005 M7.2 MIYAGI-OKI earthquake, NE Japan: Possible reactivation of one of asperities that caused the previous M7.4 earthquake. *Geophysical Research Letters*, 32, L24302. <https://doi.org/10.1029/2005GL024613>
- Okal, E. A., & Synolakis, C. E. (2015). Sequencing of tsunami waves: Why the first wave is not always the largest. *Geophysical Journal International*, 204(2), 719–735. <https://doi.org/10.1093/gji/ggv457>
- Ortiz, M., Kostoglodov, V., Singh, S. K., & Pacheco, J. (2000). New constraints on the uplift of October 9, 1995 Jalisco-Colima earthquake (M). *Geofísica Internacional*, 39(4), 349–357.
- Ortiz, M., Singh, S., Pacheco, J., & Kostoglodov, V. (1998). Rupture length of the October 9, 1995 Colima-Jalisco earthquake (Mw 8) estimated from tsunami data. *Geophysical Research Letters*, 25(15), 2857–2860. <https://doi.org/10.1029/98GL02059>
- Pacheco, J., Singh, S. K., Domínguez, J., Hurtado, A., Quintanar, L., Jiménez, Z., et al. (1997). The October 9, 1995 Colima-Jalisco, Mexico earthquake (Mw 8): An aftershock study and a comparison of this earthquake with those of 1932. *Geophysical Research Letters*, 24(17), 2223–2226. <https://doi.org/10.1029/97GL02070>
- Pacheco, J. F., Sykes, L. R., & Scholz, C. H. (1993). Nature of seismic coupling along simple plate boundaries of the subduction type. *Journal of Geophysical Research*, 98(B8), 14,133–14,159. <https://doi.org/10.1029/93JB00349>
- Pérez-Campos, X., & Beroza, G. C. (2001). An apparent mechanism dependence of radiated seismic energy. *Journal of Geophysical Research*, 106(B6), 11,127–11,136. <https://doi.org/10.1029/2000jb900455>
- Pérez-Campos, X., Singh, S., & Beroza, G. (2003). Reconciling teleseismic and regional estimates of seismic energy. *Bulletin of the Seismological Society of America*, 93(5), 2123–2130. <https://doi.org/10.1785/0120020212>
- Polet, J., & Thio, H. (2003). The 1994 Java tsunami earthquake and its “normal” aftershocks. *Geophysical Research Letters*, 30(9), 1474. <https://doi.org/10.1029/2002GL016806>
- Ramírez-Herrera, M., Bógallo, M., Černý, J., Goguitchaichvili, A., Corona, N., Machain, M., et al. (2016). Historic and ancient tsunamis uncovered on the Jalisco-Colima Pacific coast, the Mexican subduction zone. *Geomorphology*, 259, 90–104. <https://doi.org/10.1016/j.geomorph.2016.02.011>
- Reyes, A., Brune, J. N., & Lomnitz, C. (1979). Source mechanism and aftershock study of the Colima, Mexico earthquake of January 30, 1973. *Bulletin of the Seismological Society of America*, 69(6), 1819–1840.
- Sato, M., Ishikawa, T., Ujihara, N., Yoshida, S., Fujita, M., Mochizuki, M., & Asada, A. (2011). Displacement above the hypocenter of the 2011 Tohoku-Oki earthquake. *Science*, 332(6036), 1395–1395. <https://doi.org/10.1126/science.1207401>
- Seno, T., Shimazaki, K., Somerville, P., & Sudo, K. (1980). Rupture process of the Miyagi-Oki, Japan, earthquake of June 12, 1978. *Physics of the Earth and Planetary Interiors*, 23(1), 39–61. [https://doi.org/10.1016/0031-9201\(80\)90081-3](https://doi.org/10.1016/0031-9201(80)90081-3)
- Shao, G., Li, X., Ji, C., & Maeda, T. (2011). Focal mechanism and slip history of the 2011 mw 9.1 off the Pacific coast of Tohoku earthquake, constrained with teleseismic body and surface waves. *Earth, Planets and Space*, 63(7), 9. <https://doi.org/10.5047/eps.2011.06.028>
- Shapiro, N., Singh, S., & Pacheco, J. (1998). A fast and simple diagnostic method for identifying tsunamigenic earthquakes. *Geophysical Research Letters*, 25(20), 3911–3914. <https://doi.org/10.1029/1998GL900015>
- Simons, M., Minson, S. E., Sladen, A., Ortega, F., Jiang, J., Owen, S. E., et al. (2011). The 2011 magnitude 9.0 Tohoku-Oki earthquake: Mosaicking the megathrust from seconds to centuries. *Science*, 332(6036), 1421–1425. <https://doi.org/10.1126/science.1206731>
- Singh, S., Pacheco, J., Alcántara, L., Reyes, G., Ordáz, M., Iglesias, A., et al. (2003). A preliminary report on the Tecumán, Mexico earthquake of 22 January 2003 (Mw 7.4) and its effects. *Seismological Research Letters*, 74(3), 279–289. <https://doi.org/10.1785/gssrl.74.3.279>
- Singh, S., Ponce, L., & Nishenko, S. (1985). The great Jalisco, Mexico, earthquakes of 1932: Subduction of the Rivera plate. *Bulletin of the Seismological Society of America*, 75(5), 1301–1313.
- Singh, S. K., & Lerma, J. (1985). Mislocation of Mexican earthquakes as reported in international bulletins. *Geofísica Internacional*, 24(2).
- Synolakis, C. (1991). Tsunami runup on steep slopes: How good linear theory really is. *Natural Hazards*, 4(2-3), 221–234. <https://doi.org/10.1007/BF00162789>
- Tanioka, Y., & Satake, K. (1996). Fault parameters of the 1896 Sanriku tsunami earthquake estimated from tsunami numerical modeling. *Geophysical Research Letters*, 23(13), 1549–1552. <https://doi.org/10.1029/96GL01479>
- UNAM Seismology Group (1986). The September 1985 Michoacán earthquakes: Aftershock distribution and history of rupture. *Geophysical Research Letters*, 13(6), 573–576. <https://doi.org/10.1029/GL0131006p00573>
- Yamanaka, Y., & Kikuchi, M. (2004). Asperity map along the subduction zone in northeastern Japan inferred from regional seismic data. *Journal of Geophysical Research*, 109, B07307. <https://doi.org/10.1029/2003JB002683>
- Yano, T. E., Shao, G., Liu, Q., Ji, C., & Archuleta, R. J. (2014). Coseismic and potential early afterslip distribution of the 2009 Mw 6.3 L'Aquila, Italy earthquake. *Geophysical Journal International*, 199(1), 23–40. <https://doi.org/10.1093/gji/ggu241>
- Ye, L., Lay, T., Kanamori, H., & Rivera, L. (2016). Rupture characteristics of major and great ($M_w \geq 7.0$) megathrust earthquakes from 1990 to 2015: 1. Source parameter scaling relationships. *Journal of Geophysical Research: Solid Earth*, 121, 826–844. <https://doi.org/10.1002/2015jb012426>